

Force-Matching Based Polarizable and Non-Polarizable Force Fields for Perovskite and Non-Perovskite Phases of CsPbI_3

Cecilia Vona, Mathias Dankl, Ariadni Boziki, Martin P. Bircher, and Ursula Rothlisberger*

Laboratory of Computational Chemistry and Biochemistry, Ecole Polytechnique Fédérale de Lausanne (EPFL), CH-1015 Lausanne, Switzerland

E-mail: ursula.roethlisberger@epfl.ch

Phone: +41 (0)21 6930321. Fax: +41 (0)21 930320

Abstract

Lead halide perovskites have emerged as highly efficient solar cell materials. However, to date, the most promising members of this class are polymorphs, in which a wide-band gap δ phase competes with the photoactive perovskite α form, and the intrinsic physical interactions that stabilize one phase over the other are currently not well understood. Classical molecular dynamics simulations based on suitably parameterized force fields (FF) enable computational studies over broad temperature (and pressure) ranges and can help to identify the underlying factors that govern relative phase stability at the atomic level. In this article, we present a polarizable (*pol*) as well as a non-polarizable (*npol*) FF for the all-inorganic lead halide material CsPbI_3 as a prototype system exhibiting a δ/α polymorphism. Both *npol* and *pol* FFs have been determined using a force-matching approach based on extensive reference data

from first-principles molecular dynamics simulations over a wide range of temperatures. While both FFs are able to describe the perovskite as well as the non-perovskite δ phase, finer structural details as well as the relative phase stability are better reproduced with the polarizable version. A comparison of these ab initio-derived interatomic potentials allows direct insights into the physical origin of the interactions that govern the interplay between the two competing phases. It turns out that explicit polarization is the essential factor that stabilizes the strongly anisotropic δ phase over the high symmetry (cubic) perovskite α phase at lower temperatures. This fundamental difference between α and δ phase appears universal and might thus also hold for other perovskite compounds with δ/α polymorphism and thus provide rational guidance for synthetic efforts to stabilize the photoactive perovskite phase at room temperature.

1 Introduction

During the last decade, metal halide perovskites have emerged as promising light harvesting materials for next generation solar cells. In fact, the power-conversion efficiencies (PCE) of perovskite solar cells (PSCs) as registered by the national renewable energy laboratory (NREL)¹ increased from 3.8% in 2009² to 26.1% in 2023.³ These compounds share the generic stoichiometric formula ABX_3 and consist of a divalent metal cation ($B = \text{Pb}^{2+}$ or Sn^{2+}), a halide anion ($X = \text{I}^-$, Br^- , Cl^-) and a monovalent cation which can be an organic molecular ion such as $A = \text{methylammonium}$ ($\text{MA} = \text{CH}_3\text{NH}_3^+$), or formamidinium ($\text{FA} = \text{CH}(\text{NH}_2)_2^+$), or an inorganic elemental ion such as $A = \text{Cs}^+$. The current record efficiencies for single-junction PSCs are based on the perovskite phase of FAPbI_3 that features a nearly ideal band gap of 1.44 eV⁴ and exhibits increased thermal stability with respect to MAPbI_3 . However, one drawback of FAPbI_3 is that the photovoltaically active perovskite α phase is not the most thermodynamically stable form at room temperature, at which the compound assumes a δ polymorph that is a wide band gap semiconductor unsuitable for use as an efficient solar light absorber. The same type of polymorphism also occurs in the case of the all-inorganic

CsPbI₃ material, which has become an ideal material for tandem solar cells^{5,6} and light-emitting diodes⁷ thanks to its optical properties along with relatively easy synthesis. The question of how to control the phase transition of these compounds and stabilize the α phase is an intensely researched topic and several strategies have been devised for this purpose. Among these, there are the use of mixtures of monovalent cations such as FA/MA and FA/Cs mixed compounds, mixed 2D/3D perovskites⁸⁻¹¹ and the use of additives.¹²⁻¹⁴ However, the preparation of phase-pure and long-term stable α phase remains an issue.¹⁵

In principle, computer simulations could help in deciphering the factors that influence the relative stability and transition between the two phases and thus give important guidance for suitable and rational synthesis approaches. This task can only be achieved by a computational method that can reliably predict the relative finite temperature stability of the competing phases and allow the treatment of sufficiently large sample sizes (and time scales) to avoid artifacts due to finite size effects and/or limited sampling of thermally relevant configurations. These requirements are hard to fulfill at the level of a full first-principles, e.g. density functional theory (DFT) based description, but can more easily be provided when using suitably parameterized force fields (FF). Not surprisingly, considerable research efforts have been directed at the development of accurate FFs for lead halide perovskites. One of the first FFs (MYP0) was developed by Mattoni et al. for MAPbI₃.¹⁶ It adopts three related perovskite phases (orthorhombic, tetragonal and cubic) as a function of temperature while no δ phase has so far been reported for this system. However, the first-generation MYP0 FF fails to describe the room temperature tetragonal phase. MYP0 has been modified¹⁷ and extended to remedy this shortcoming and to describe the interaction of MAPbI₃ with water¹⁸ as well as to capture MAPbBr₃ and mixed halide MAPbI_{3-x}Br_x compounds.¹⁹ Alternatively, DFT-trained machine-learning potentials (MLPs) for MAPbI₃, MAPbBr₃ and MAPbCl₃ have been generated.^{20,21} While the relative stabilities and the transition between different perovskite-like polymorphs can be described fairly well with several of the current FFs, the simultaneous description of the non-perovskite δ phase and the perovskite phase(s)

and the transition between the photovoltaically active and inactive phases, respectively, has remained challenging and the authors are not aware of any attempts made so far to develop such FFs.

Here, we will focus on the most simple prototypical compound that exhibits the emergence of a competing δ phase, the all-inorganic CsPbI₃, with the goal of developing accurate ab initio derived FFs that can simultaneously describe both phases and allow insights into the factors that govern relative phase stability. CsPbI₃ exhibits a first-order phase transition from the δ to the cubic α perovskite phase at about 600K^{22,23} and upon cooling can be trapped into tetragonal (β) and orthorhombic (γ) metastable perovskite phases.²⁴ Apart from its structural properties, the perovskite phase of CsPbI₃ (and its mixed halide counterparts) possesses a tunable band gap in the range of 1.72 - 2.3 eV,²⁵ strong absorption and high photoluminescence quantum yield in the red²⁶ which makes it highly suitable for many optoelectronic applications. Not surprisingly, several attempts to develop FFs or MLPs for this system have been undertaken. A recently developed reactive FF targeted at describing the decomposition of CsPbI₃ into PbI₂ and CsI focuses on capturing the different perovskite phases of the system; however, it does not take the thermodynamically most stable form at room temperature, i.e. the δ phase into account,²⁷ which is similar to a recent MLP.²⁸ A hybrid Embedded Atomic Buckingham - Coulomb (EABC) potential is able to accurately reproduce the density and structural properties of the orthorhombic δ phase of CsPbI₃ but does not seem to yield the transformation to the high-temperature α phase²⁷ which has also been reported for the polarizable FF developed by Rathnayake et al.²⁹ To the best of our knowledge, so far, no computational approach has successfully described the transition from the δ to the perovskite phase within a single molecular dynamics simulation. However, a theoretical estimate of the transition temperature has been obtained by a combination of ab initio electronic structure calculations with vibrational entropy contributions modeled via a SchNetPack deep learning potential trained on ab initio MD data.³⁰

In view of its simplicity and lower computational effort, it seems worthwhile to fully

explore the performance limits of polarizable as well as unpolarizable FFs for this system. Here, we generate optimal nonpolarizable (*npol*) as well as polarizable (*pol*) models using an automated procedure based on a force-matching (FM) approach³¹ in which the freely-adjustable parameters of both FF variants are fitted in such a way as to minimize the difference between the forces acting on all atoms with those from first-principles (DFT) based molecular dynamics simulations of both α and δ phases, covering extended time scales and temperature ranges. By using the same reference data for both models, we can directly assess the additional benefits that can be achieved via a fully polarizable version and gain further insights into the factors that govern the relative phase stability.

2 Methods

2.1 Nonpolarizable and polarizable interatomic potentials

The functional form that we have chosen to represent both *npol* and *pol* versions of the interatomic potential for CsPbI₃ is the one of the **A**tomic **M**ultipole **O**ptimized **E**nergetics for **B**iomolecular **A**pplications (**AMOEB**A) FF as implemented in the **TINKER** package version 7.1.³²⁻³⁴ Originally designed for biomolecular applications, AMOEBA is a next-generation FF with a flexible form and a highly accurate and transferable representation of electrostatic interactions. Metal halide perovskites are known to be soft materials in which polarization effects can play an important role.³⁵ This special property makes them suitable for charge carrier transport,³⁶ but it is also one of the causes of their structural instability. Aiming at the development of high-accuracy FFs for these materials, it seems pertinent to include the possibility of polarization effects to assess their potential impact on structural, energetic and dynamic properties.

In CsPbI₃, the only contributions to the interatomic potential are from van der Waals (vdW) and electrostatic interactions:

$$U(r_{ij}) = U_{\text{vdW}}(r_{ij}) + U_{\text{el}}(r_{ij}). \quad (1)$$

The electrostatic term in the AMOEBA FF includes two components, one describing contributions due to permanent electrostatic interactions and the other due to induced dipoles and quadrupoles, $U_{\text{el}} = U_{\text{el}}^{\text{perm}} + U_{\text{el}}^{\text{ind}}$. $U_{\text{el}}^{\text{perm}}$ describes the electrostatic interactions between atom-centered multipoles $\mathbf{M} = [q, \mu_x, \mu_y, \mu_z, Q_{xx}, Q_{xy}, Q_{xz}, \dots, Q_{zz}]^T$, where q is the atomic charge, $\boldsymbol{\mu}$ is the (permanent) dipole and \mathbf{Q} the (permanent) quadrupole moment. On the other hand, $U_{\text{el}}^{\text{ind}}$ describes the electronic polarization that is attributed to the distortions of the electronic density under the influence of an external field originating from the charges in the system. The total dipole and quadrupole moments are the sum of the permanent and the induced contributions, $\boldsymbol{\mu} = \boldsymbol{\mu}^{\text{perm}} + \boldsymbol{\mu}^{\text{ind}}$ and $\mathbf{Q} = \mathbf{Q}^{\text{perm}} + \mathbf{Q}^{\text{ind}}$, respectively. The electrostatic interaction between two atomic centers i and j is expressed as follows:

$$U_{\text{el}}(r_{ij}) = \mathbf{M}_i^T \mathbf{T}_{ij} \mathbf{M}_j. \quad (2)$$

In this expression r_{ij} is the distance between the two atomic centers and \mathbf{T}_{ij} is the multipole interaction matrix:

$$\mathbf{T}_{ij} = \begin{pmatrix} T_{ij} & T_{ij,x} & T_{ij,y} & T_{ij,z} & \dots \\ T_{ij,x} & T_{ij,xx} & T_{ij,xy} & T_{ij,xz} & \dots \\ T_{ij,y} & T_{ij,yx} & T_{ij,yy} & T_{ij,yz} & \dots \\ T_{ij,z} & T_{ij,zx} & T_{ij,zy} & T_{ij,zz} & \dots \\ \vdots & \vdots & \vdots & \vdots & \ddots \end{pmatrix}, \quad (3)$$

where the matrix elements are $T_{ij} = (r_{ij})^{-1}$, $T_{ij,\alpha} = \partial_{\beta} T_{ij}$ and $T_{ij,\beta\gamma} = \partial_{\beta} T_{ij,\beta}$ where $\beta, \gamma = x, y, z$ (in the Supporting Information \mathbf{T}_{ij} is given in an explicit form). When the interactions involve induced dipoles and quadrupoles they have to be damped to avoid the *polarization catastrophe*, which can occur at very short range.³⁷ This damping results in the

introduction of a smearing function for the charge defined as:

$$\rho = \frac{3a}{4\pi} e^{-aw^3}, \quad (4)$$

in which $u = r_{ij}/(\alpha_i\alpha_j)^{1/6}$ is the effective distance as a function of atomic polarizabilities of sites i and j , namely α_i and α_j , respectively and a is the damping factor.

In contrast to organic-inorganic lead halide perovskite materials such as MAPbI₃ and FAPbI₃, in the case of CsPbI₃, that is purely constituted of elemental ions, there are no permanent atomic dipoles and quadrupoles. The induction part however still plays a role in CsPbI₃ as a consequence of structural anisotropies and finite temperature distortions. In the AMOEBA FF, the induced dipole $\boldsymbol{\mu}^{\text{ind}}$ is evaluated self-consistently as follows:

$$\mu_{i,\beta}^{\text{ind}} = \alpha_i \left(\sum_{\{j\}} T_{ij,\beta} \mathbf{M}_j + \sum_{\{j'\}} T_{ij',\beta\gamma} \mu_{j',\gamma}^{\text{ind}} \right) \quad \text{for} \quad \beta, \gamma = x, y, z. \quad (5)$$

Here the set of atomic coordinates $\{j\}$ includes all the atomic sites outside the molecule which contains i , whereas the set of atomic coordinates $\{j'\}$ contains all the atomic sites except i itself. In the case of CsPbI₃ the induced dipole equation simplifies to $\mu_{i,\beta}^{\text{ind}} = \alpha_i [\sum_{\{j\}} T_{ij,\beta} q_{ij} + \sum_{\{j'\}} T_{ij,\beta\gamma} \mu_{j,\gamma}^{\text{ind}}]$.

For the van der Waals interaction term U^{vdW} , we use a Lennard-Jones (LJ) potential with parameters ϵ_{ij} and σ_{ij} , as opposed to other possible choices such as Buckingham³⁸ or Hill potentials.³⁹ These three interatomic potentials differ in their repulsive parts, which could have an effect on e.g. the interaction between nearest I-Pb ions that lie in a typical range of 3.1-3.5 Å in lead halide perovskite materials.⁴⁰ However, it turns out that the functional form of the LJ potential appears to have sufficient flexibility to achieve close matches between the FF forces and the first-principles reference data.

Taken all together for the case of CsPbI₃, the *pol* FF, has the following form:

$$U^{\text{pol}}(r_{ij}) = 4\varepsilon_{ij} \left[\left(\frac{\sigma_{ij}}{r_{ij}} \right)^{12} - \left(\frac{\sigma_{ij}}{r_{ij}} \right)^6 \right] + \frac{1}{4\pi\varepsilon_0} \left[\frac{q_i q_j}{r_{ij}} - q_i \frac{\mathbf{r}_{ij} \cdot \boldsymbol{\mu}_j^{\text{ind}}}{r_{ij}^3} - q_j \frac{\mathbf{r}_{ij} \cdot \boldsymbol{\mu}_i^{\text{ind}}}{r_{ij}^3} + (\boldsymbol{\mu}_i^{\text{ind}})^T \mathbf{T}'_{ij} (\boldsymbol{\mu}_j^{\text{ind}}) \right]. \quad (6)$$

Here $\boldsymbol{\mu}_{ij}^{\text{ind}} = [\mu_{ij,x}, \mu_{ij,x}, \mu_{ij,x}]^T$ and \mathbf{T}'_{ij} is a 3×3 matrix composed by elements with form $T_{ij,\beta\gamma}$. For the *npol* variant, we use the same functional form given in Eq. 6 but omit all the terms involving $\boldsymbol{\mu}^{\text{ind}}$.

2.2 Fitting procedure

To determine the parameters of the *npol* and *pol* FFs for CsPbI₃, a FM approach has been employed. Originally introduced by Ercolessi and Adams in 1994,³¹ this method is a powerful approach to directly construct interatomic potentials from first-principles calculations in a semi-automated way. The central idea is the minimization of an objective function, which in the current work is defined as follows:

$$\tau_{\text{F}}(\{\boldsymbol{\sigma}\}) = \left(\sum_{k=1}^{\text{M}} \text{N}_k \right)^{-1} \sum_{k=1}^{\text{M}} \sum_{i=1}^{\text{N}_k} \left| \mathbf{F}_{ki}(\{\boldsymbol{\sigma}\}) - \mathbf{F}_{ki}^0 \right|^2. \quad (7)$$

In this non-linear least squares problem, the goal is to determine the set of parameters $\{\boldsymbol{\sigma}\}$ which minimize the difference between the forces from first-principles \mathbf{F}_{ki}^0 and the forces $\mathbf{F}_{ki}(\{\boldsymbol{\sigma}\})$ that are constructed from the interatomic potential employing the set of parameters $\{\boldsymbol{\sigma}\}$. The first-principles reference forces are generated from DFT molecular dynamics runs at different temperature and pressure conditions. Therefore, in Eq. 7, the index $k = 1, \dots, \text{M}$ denotes the trajectory frame under consideration with M being the total number of frames, and the index $i = 1, \dots, \text{N}_k$ represents the atom in frame k where N_k is the total number of atoms (in frame k) included in the fitting procedure. Therefore $(\sum_{k=1}^{\text{M}} \text{N}_k)^{-1}$ is the normalization factor, i.e. the inverse of the total number of atomic forces for all atoms and

frames that are used for the fitting.

Other physical quantities, like e.g. energies and bulk moduli, can also be included in the objective function in addition to the forces themselves.^{31,41} However here, we opted for a purely force-based objective function as given in Eq. 7.

For the practical implementation of the FM approach, an interface between a classical molecular dynamics and a minimization package has to be developed. For the latter, the minimization package MINPACK^{42,43} was selected, which offers numerically stable subroutines to solve linear and non-linear least squares problems, while for the former the classical molecular dynamics software TINKER^{33,34} was adopted, which was originally designed for the polarizable AMOEBA FF but enables also the use of a variety of other FFs. In this way, at each iteration I , the classical forces $\mathbf{F}_{ki}(\{\boldsymbol{\sigma}^I\})$ are computed with a given set of parameters $\{\boldsymbol{\sigma}^I\}$ by TINKER and then used to compute the modulus squared of the force difference $|\mathbf{F}_{ki}(\{\boldsymbol{\sigma}^I\}) - \mathbf{F}_{ki}^0|^2$ as a contribution to the objective function in Eq. 7 that at the end of the iteration is minimized with a Levenberg-Marquardt algorithm from MINPACK to determine a new set of parameters $\{\boldsymbol{\sigma}^{I+1}\}$. This iterative process is pursued until the convergence parameters of MINPACK lie below 10^{-9} .

2.3 Computational details

2.4 Static DFT Calculations

To determine the supercell size and to optimize the cell and geometry of the δ and α phase of CsPbI₃, we employed the Quantum ESPRESSO (QE) package version 6.0.⁴⁴ DFT calculations were performed with the exchange-correlation functional by Perdew, Burke and Ernzerhof (PBE).⁴⁵ For Pb and I, we used pseudopotentials of the Rappe-Rabe-Kaxiras-Joannopoulos type,⁴⁶ while, for Cs, which has only one valence electron, we used an ultrasoft pseudopotential of Vanderbilt type.⁴⁷ The plane wave cutoff selected for the expansion of the wavefunction and charge density are 50 Ry and 400 Ry, respectively, each determined

employing a convergence criterion of $\sim 10^{-3}$ Ry per stoichiometric unit (s.u.) for the total energy. To determine the supercell sizes we made use of k-point sampling and adopted convergence criteria of $\sim 10^{-3}$ Ry on the total energy per stoichiometric unit (s.u.) and $\sim 10^{-4}$ Ry/a.u. for the atomic forces. Cell and geometry optimizations have been performed on supercells of sizes 2x4x1 for δ CsPbI₃ (160 atoms) and 4x4x3 for α CsPbI₃ (240 atoms) constructed from the experimental unit cell of Ref.⁴ and Ref.,⁴⁸ respectively. In the remainder of the manuscript, the cell volumes obtained through optimizations are referred to as V_0 . In order to include higher flexibility in the FM procedure, we also considered additional supercells with a different volume, which we refer to as V_1 . The latter cells were constructed by isotropical expansion of the 0K optimized δ and α phase lattices by 5% on each axis. The cell volume and lattice parameters are summarized for the two phases in Table 1.

2.4.1 Generation of first-principles MD trajectories

Using Car-Parinello (CP) molecular dynamics within the CPMD software version 4.1,⁴⁹ trajectories have been generated in the NVE ensemble for α CsPbI₃ at an average temperature of 650 K and for δ CsPbI₃ at 100, 300 and 500 K, for both volumes V_0 and V_1 using the PBE exchange-correlation functional and pseudopotentials of Goedecker-Teter-Hutter type.⁵⁰⁻⁵² A cutoff of 90 Ry was used for the plane-wave expansion of the Kohn-Sham orbitals determined by applying a convergence criterion of $\sim 10^{-3}$ Ry per s.u. for the total energy. Before starting the MD, we performed an additional geometry optimization with the CPMD software. The time step adopted for the CP dynamics was 5 a.u. and the fictitious electron mass was set to 800 a.u. The systems were first equilibrated at the different temperatures applying a Nosé-Hoover thermostat^{53,54} with a coupling frequency of 1000 cm⁻¹ for ~ 1 ps followed by NVE runs of the equilibrated systems of ~ 7 ps. From these trajectories, we collected the frames to perform the FM.

Table 1: Optimized (0K) cell dimensions of the α and δ phases compared with the experimental unit cell. In CP trajectories and NVT classical trajectories, the same cell is used at finite temperature, while for NPT trajectories information about the volume variation at finite temperature is given in the Supporting Information. Cell dimensions are given in terms of the number of unit cells replicated in each direction, and ΔV % stands for the relative difference of the volume per s.u. with respect to the experimental one. RMSD is the root mean square deviation from the experimental structure.

α phase					
	Experimental ⁴⁸	DFT-V ₀	DFT-V ₁	<i>npol</i>	<i>pol</i>
(super)cell size	1x1x1	4x4x3	4x4x3	7x7x7	7x7x7
a=b [Å]	6.29	25.43 (6.36)	26.70	43.63 (6.23)	43.88 (6.27)
c [Å]	=a=b	19.36 (6.45)	20.33	=a=b	=a=b
V per s.u. [Å ³]	248.86	260.83	301.94	242.14	246.32
ΔV %	-	+5%	+21%	-3%	-1%
RMSD [Å]	-	0.45	-	0.20	0.08
δ phase					
	Experimental ⁴	DFT-V ₀	DFT-V ₁	<i>npol</i>	<i>pol</i>
(super) cell size	1x1x1	2x4x1	2x4x1	4x8x2	4x8x2
a [Å]	10.43	21.60 (10.80)	22.68	40.55 (10.14)	42.78 (10.70)
b [Å]	4.79	19.56 (4.89)	20.54	40.12 (5.02)	38.90 (4.86)
c [Å]	17.76	18.25	19.16	36.43 (18.22)	35.21 (17.61)
V per s.u. [Å ³]	221.82	240.95	278.93	231.51	228.88
ΔV %	-	+9%	+26%	+4%	+3%
RMSD [Å]	-	0.29	-	0.78	0.39

Force matching

To perform the FM, we used the interface between the MINPACK-1 package^{42,43} and TINKER³⁴ described in the section about the fitting procedure. The input forces are collected from a total of 60 frames: 12 frames for each of the two α phase trajectories each containing 240 atoms, and 6 frames for each of the six δ phase trajectories with 160 atoms each. With this choice, 2880 forces are given as input to the interface for the α phase and the same number for the δ phase. The frames have been sampled equidistantly with an interval of 0.48 ps. To verify that the number of frames was sufficient, we also performed the FM for a smaller and a larger number of frames, and no substantial differences were observed. To obtain accurate forces as input for the FM interface, we performed for each frame an additional self-consistent DFT cycle employing a larger plane wave cutoff for the wave function

expansion of 110 Ry. In addition to the forces, initial guesses of the FF parameters have to be given as an input. For this, we started using parameters of existing FFs such as the two sets of parameters developed by Mattoni and coworkers for MAPbI₃,^{16,18} re-scaled parameters coming from MgSiO₃,^{55,56} and parameters given by single ions interacting with solvent.^{57,58} The fitting procedure was started from several different sets of initial parameters and the chosen final result was the one that led to i) the minimal root-mean-square deviation of the force magnitude⁵⁹

$$|\Delta\mathbf{F}|_{\text{rms}} = \sqrt{\sum_{k=1}^M \sum_{i=1}^{N_k} \omega_{ki} \left(\frac{|\mathbf{F}_{ki}^{\text{FF}}| - |\mathbf{F}_{ki}^0|}{|\mathbf{F}_{ki}^0|} \right)^2}, \quad (8)$$

where $|\mathbf{F}_{ki}^{\text{FF}}|$ is the magnitude of the forces computed with the FF model and ω_{ki} the weight that depends on the magnitude of the DFT forces:

$$\omega_{ki} = \frac{|\mathbf{F}_{ki}^0|}{\sum_{k'=1}^M \sum_{i'=1}^{N_{k'}} |\mathbf{F}_{k'i'}^0|}. \quad (9)$$

and that ii) Minimized the angular deviation of the force directions

$$\theta_{\text{avg}} = \sum_{k=1}^M \sum_{i=1}^{N_k} \omega_{ki} \theta_{ki}, \quad (10)$$

where θ_{ki} is the angle between the DFT forces and the forces computed with the FF model. As a first test of the resulting FF, the relative energetic ordering at 0 K of the δ phase with respect to the α phase was determined. For this, the total energy for each phase was computed with TINKER after optimizing the cell and geometry with a given set of FF parameters. More details about this procedure are given in the next section.

Overall we observed that the vdW parameters resulting from the FM procedure are very sensitive to the choice of the input parameters, while the electrostatic parameters are more stable.

With this fitting procedure, we developed a polarizable FF for CsPbI₃ with the form given in Equation 6 (*pol* model) and a fixed-point charge (*npol* model) FF, which includes

only the permanent electrostatic potential. In total, we determined 16 parameters for the *pol* FF and 13 for the *npol* FF. Since, the effect of the damping factor a is likely to be of minor importance in a crystal like CsPbI₃, we did not include this parameter in the fit. Instead, we used its default value of 0.39.⁶⁰ Charge neutrality was imposed during the fit by setting $q_{\text{Cs}} = q_{\text{Pb}} + q_{\text{I}}$. The vdW parameters σ and ϵ have been determined explicitly for the Pb-I and Cs-I pair interactions, while for Cs-Pb, they are computed internally by TINKER via the Lorentz-Berthelot mixing rules:

$$\sigma_{\text{PbCs}} = \frac{\sigma_{\text{Pb}} + \sigma_{\text{Cs}}}{2}, \quad \epsilon_{\text{PbCs}} = \sqrt{\epsilon_{\text{Pb}}\epsilon_{\text{Cs}}}. \quad (11)$$

This is justified by the larger interatomic distance between Cs-Pb, which leads to relatively small vdW contributions without a major impact on the fitting results.

2.4.2 FF based MD runs

All classical MD simulations were performed with the TINKER code.³⁴ For the *npol* model, we used a vdW cutoff (R_{vdW}) of 17 Å and a real-space cutoff (R_{EW}) for the Ewald summation of the electrostatic interactions of 6 Å. For the *pol* model, R_{EW} was the same while $R_{\text{vdW}}=16$ Å. The system size was chosen in such a way as to respect the minimum image convention, i.e. the edge of the supercell was at least double the largest cutoff used in the simulation. The simulation systems thus contained 4x8x2 (1280 atoms) for the δ phase and 7x7x7 (1715 atoms) for the α phase. Before performing MD simulations, we optimized the cell and the geometry and used the total energy of the fully optimized systems to determine the energetic ordering of the two phases at 0 K. For the α phase we also obtained an optimized structure starting from frames generated from the NPT trajectories at 100K. We performed the cell and coordinate optimizations for frames at 0.1 ns intervals and we chose the one lowest in energy. The use of so few frames is justified by the small order of magnitude of energy difference (below 0.02 kcal/mol per s.u.) between the obtained optimized structures. To

assess the performance of the developed *pol* and *npol* FFs at finite temperature, we generated trajectories for the α and δ phase at 100 K, 300 K, 500 K, 600 K and 650 K, in the NVT and NPT (with $P=1$ atm) ensembles. For temperature control, the Bussi thermostat with a coupling time of 0.1 ps and a Monte Carlo barostat with a coupling time of 2 ps were used. The employed time step was 2 fs and after equilibration, trajectories were run for 1 ns.

2.4.3 Evaluation of system properties

Comparison with Bader charges

For each ab initio trajectory, the coordinates of twelve snapshots were taken at equidistant time intervals of 0.48 ps and Gaussian CUBE files were generated from the optimized density using the *PostProc* package from QE version 6.6.^{44,61,62} The density used for generating the cube file was computed using the PBE functional⁴⁵ with a wavefunction cutoff of 90 Ry and a charge density cutoff of 720 Ry as well as employing a 3x3x3 Monkhorst k-point grid. The pseudopotentials are the same as described in Sec 2.4. From the obtained cube files Bader charges were computed using the program developed by Henkelman et al.⁶³

Analysis of structural and energetic properties

We analyzed the radial pair distribution functions (RPDF) for all the different pairs of atoms, for both the optimized supercells at 0K and the trajectories at finite temperature. We compute the RPDF with VMD,⁶⁴ considering spherical slices of bin size 0.1 Å at finite temperature and 0.01 Å at 0K. For the DFT trajectories, we considered equidistant frames taken every 1.2×10^{-2} ps and for the classical trajectories every 1 ps. To analyze the energies and the volumes of the classical trajectories at finite temperature, we computed the time average from frames taken every 1 ps.

Analysis of vibrational properties

To compute the CsPbI₃ power spectra we made use of the TRAVIS code.⁶⁵ For the DFT

trajectories, we analyzed 550 frames taken every 1.2×10^{-2} ps while for the classical MD we used a time interval of 0.1 ps. In both cases, the autocorrelation function has been weighted with respect to the atomic masses. For a better comparison of the shape of the power spectra at different temperatures, the spectra have been normalized to 1. Additionally, we smoothed the power spectra generated by the Travis code for the classical trajectories employing the Gaussian filter as implemented in Scipy with `sigma=20`.

3 Results and discussion

3.1 Force-matched force fields

The parameters obtained from the FM procedure for the *pol* (Eq. 6) and *npol* FF are summarized in Table 2. At difference to its *npol* counterpart, the *pol* model also includes the

Table 2: Parameters of the *pol* and *npol* FFs for CsPbI₃ obtained via FM.

	<i>pol</i>				<i>npol</i>		
	σ [Å]	ϵ [kcal/mol]	q [e]	α [Å ³]	σ [Å]	ϵ [kcal/mol]	q [e]
Pb	5.1647	0.1140	1.1860	2.720	4.8620	0.1271	0.8589
Cs	4.2631	0.3295	0.7919	0	3.4910	3.4422	0.7680
I	4.6452	0.0544	-0.6593	5.050	4.6121	0.0611	-0.5423
Pb-I	3.9357	0.0620	-	-	3.8623	0.0499	-
Cs-I	4.2053	0.1448	-	-	4.2024	0.1403	-

interactions between atomic charges and induced dipoles as well as the interactions among induced dipoles. As shown in Eq. 5, the induced dipole is proportional to the polarizability α , which is the only additional parameter of the *pol* FF. For both FFs, the resulting effective atomic charges are quite far from the values for the fully isolated ions ($q_{\text{Pb}}=+2$ e, $q_{\text{Cs}}=+1$ e and $q_{\text{I}}=-1$) but show a good agreement with average Bader charges computed from the electron density distributions along the DFT trajectories ($q_{\text{Pb}}=+0.936 \pm 0.018$ e, $q_{\text{Cs}}=+0.839 \pm 0.015$ e and $q_{\text{I}}=-0.592 \pm 0.007$ e). In fact, for Pb and I, the calculated Bader charges are in between the effective charges of the *pol* and *npol* models while the one of Cs is slightly larger in both FFs, but the difference between the three values is within 0.1 e. Moreover, the

differences of the averaged Bader charges obtained for the individual phases, temperatures and cell sizes, are as small as 0.048 e for all three ions (values in the Supporting Information), which is a first indication that, at least from an electrostatic point of view, a single FF model should indeed be able to simultaneously reproduce the different phases of CsPbI₃ at finite temperature.

The experimental values of the polarizabilities are 2.44 Å³ for Cs⁺, 7.16 Å³ for I⁻⁶⁶ and 2.02 Å³ for Pb²⁺.⁶⁷ Our parameters do reproduce the physical trend between Pb²⁺ and I⁻, although, for the latter, the atomic polarizability is around 2 Å³ smaller. The largest difference exists for Cs⁺, which in the FF case has zero polarizability. This might be due to the fact that the Cs ions are free to move within the Pb-I cages, and the induced dipole moment might be partially cancelled out by their thermal motion.

The vdW interactions were fitted using 10 parameters for both FFs (2 for each of the 3 species and another 4 for the explicitly treated Pb-I and Cs-I pair interactions). As already mentioned, the fitting procedure is less sensitive to the values of the (weaker) van der Waals interactions and the resulting σ and ϵ values follow less of a physical trend than the effective charges.

Overall, in the *npol* case, the objective function in Eq. 7 could be minimized down to a relative average error between first-principles and FF forces of $|\Delta F|_{\text{rms}} = 39.5\%$ and an angular deviation of the force directions of $\theta_{\text{avg}} = 26.8^\circ$, whereas for the *pol* model, the deviations are further reduced to $|\Delta F|_{\text{rms}} = 32.7\%$ and $\theta_{\text{avg}} = 16.6^\circ$. These errors lie in a range typically observed for the FM procedure.^{41,59} Comparing the two FFs, the *pol* model clearly shows a lower error than *npol*. Particularly interesting is the decrease of 10.2° in the directional force error θ_{avg} , which might be a reflection of the fact that the *pol* FF accounts for anisotropic charge distributions.

3.2 Zero Kelvin Properties

3.2.1 Structural properties at 0K

The FF parameters obtained with the FM method (Table 2) have been used to optimize the cell and the geometry of the α and δ phases and the results are given in Table 1. To assess the predictive performance of the FF in describing the α and δ structure, we use the experimental structure as the reference (Table 1). However, since the FF parameters were fitted based on DFT data, the theoretical performance of the FF should also be judged with respect to the DFT data. For the α phase, the FFs generate 0K optimized cells with slightly smaller volumes per s.u. than the one of the experimental unit cell (measured at 634 K) with deviations of -3% and -1% for the *npol* and the *pol* models, respectively. The volume of the δ phase measured at room temperature is slightly larger, showing an increase of +4% with the *npol* model and +3% with the *pol* model. In both cases, the obtained deviations are smaller than the ones of the DFT optimizations which are +5% for the α phase and +9% for the δ phase. Although both FFs seem to reproduce the overall volume of the experimental α and δ phase in a comparable manner, if one takes into account the individual unit cell axes (Table 1, results in parenthesis), one can observe that the contraction of the α phase volume is isotropic, in contrast with the δ phase, in which some of the axes expand and others contract. The opposite is observed with the DFT method, in which in the α phase the axes become inequivalent, most probably as an artifact of the anisotropic shape of the supercell chosen to reduce computational cost. The root mean square displacement (RMSD) between the experimental and the optimized structures averaged over all the supercells (Table 1), computed with the VMD software,⁶⁴ shows for the α phase the same trend as for the volume deviation, with the DFT geometry having the worst agreement. In contrast, for the δ phase the trends do not coincide, e.g., the DFT geometry has the smallest RMSD but the largest volume expansion. The worst agreement is obtained for the δ phase structure optimized with the *npol* model. An idea about the atomistic origin of this disagreement can

be obtained from an analysis of the radial pair distribution functions (RPDFs). While most of the RPDFs are in close agreement (Figure S1 in the Supporting Information), some larger peak displacements among the different models are observed for Pb-I, Pb-Pb and Pb-Cs pairs in the δ phase (Figure 1). In fact, from the RPDFs of Pb-I shown in Figure 1a, it is evident that all models agree relatively closely with respect to the position of the first peak (corresponding to the length of the Pb-I bonds) but there are clear differences in the location of the second-nearest neighbor interactions, where the *npol* model has three small peaks at $\sim 4.9\text{\AA}$, which is displaced by as much as $\sim 0.5\text{\AA}$ from the position of the second coordination sphere of the other models. A similar discrepancy is observed for the second shell of the Pb-Pb RPDFs, where the peaks usually situated around $\sim 8\text{\AA}$ are displaced by $\sim 1\text{\AA}$ to $\sim 7\text{\AA}$ in the *npol* model, and in the Cs-Cs RPDFs where the second-coordination shell peak that should be located at $\sim 6\text{\AA}$ is at $\sim 5.5\text{\AA}$ instead, whereas the peak that should be centered at $\sim 6.8\text{\AA}$ is displaced in the opposite direction by $\sim 0.7\text{\AA}$ (to $\sim 7.5\text{\AA}$). These differences in the RPDFs are the consequences of changes in the relative distances between edge-sharing octahedral pillars of the δ phase and the Cs ion displacements in the interoctahedral spaces as visualized in Figure 1b. This figure shows that pairs of Cs ions such as the two highlighted in magenta get closer together (by 0.33\AA with respect to the experimental reference) while those equivalent to the one in blue are further separated (by 0.80\AA). Nevertheless, even though the structure is not reproduced in all fine details, it retains the overall characteristics of the CsPbI_3 δ phase, in which the octahedra are edge-sharing. In the next section, we will show that the deviation of the optimized δ phase structure obtained with the *npol* FF also leads to some discrepancies in the finite temperature properties.

In contrast, regarding the α phase, the RPDFs of all models are in good agreement as shown in Figure S2 in the Supporting material.

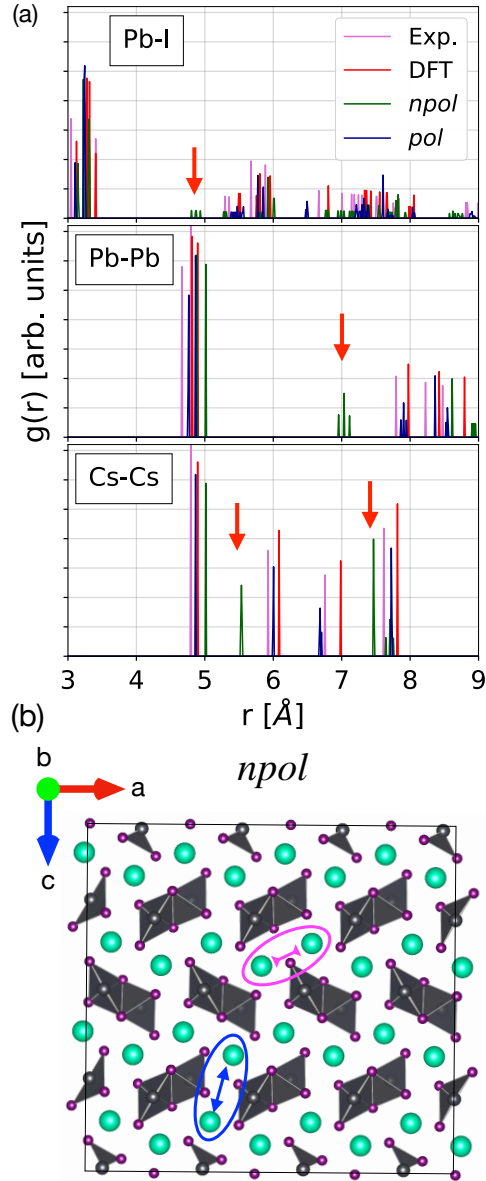


Figure 1: Structural properties of the optimized δ phase: (a) RPDFs of the δ phase optimized using DFT and the $npol$ and pol FFs compared to the experimental RPDFs for the pairs Pb-I, Pb-Pb and Cs-Cs. The red arrows indicate peaks obtained with the $npol$ model with the largest deviations in comparison to those from other levels of theory and experiments. (b) $npol$ atomistic structure. The red arrow shows the deviations in the separation of face-sharing octahedral pillars. The Cs-pairs highlighted in magenta get closer in the $npol$ structure while the pair indicated in blue are separated further apart.

3.2.2 Energy analysis at 0K

The newly-developed FFs reproduce the correct energetic ordering of the two phases when optimized starting from experimental structures^{4,48} with the δ phase being more stable than the α phase. The energy difference between the δ and α phases at the *ab initio* level is taken as reference with $\Delta E = E_\alpha - E_\delta = 3.90$ kcal/mol per s.u.. The polarizable model reproduces the energy difference in excellent agreement ($\Delta E = 3.99$ kcal/mol per s.u.) while the *npol* model yields the correct energetic order but clearly underestimates the energy difference ($\Delta E=0.36$ kcal/mol per s.u.). From an analysis of the total energy as a function of temperature (see Sec. 3.3.3) (that in general follows a roughly linear trend), we realized that the FF-optimized α phase structure obtained from the experimental data likely corresponds to a local minimum. In fact, by optimizing the structure starting from frames of the NPT trajectories at 100 K, due to symmetry breaking of the perfectly cubic experimental structure, we obtain a structure that is lower in energy and that presents an axes ratio and octahedral tilting reminiscent of the orthorhombic phase (Supporting Information). In the *npol* FF, due to the small energy difference between the two phases, this new orthorhombic structure leads to a reversal of the energetic ordering between α and δ phases. In contrast, in the *pol* model the energy difference is reduced by 1.57 kcal/mol per s.u. but the ordering is maintained. This reduction should not be interpreted as a disagreement with respect to the DFT reference, which was itself optimized starting from the highly-symmetric cubic experimental structure.

Details of the energetics of the two phases, including the α phase structures optimized from 100K trajectories frames, are given in Table 3, in which the values and the differences of the total energy and its components, such as vdW (E_{vdW}), permanent electrostatic components ($E_{\text{el,perm}}$) and the induced electrostatic contribution ($E_{\text{el,ind}}$) of the polarizable model are shown.

Not surprisingly, the contributions from electrostatic interactions are dominant but due to the small energy difference between the phases, the vdW interactions can become of

comparable influence and can have a decisive effect in some cases. In fact, in both models, the vdW contribution is destabilizing the α phase and favoring the δ phase, thus counteracting the permanent electrostatic contribution. In the *npol* model, vdW and electrostatic energy difference contributions are of similar size (though with opposite signs). In the FF re-optimized experimental structures, the former is slightly larger leading to a more stable δ phase, while for the new minimum of the α structure derived from the 100 K dynamics, the opposite is the case. In the *pol* model on the other hand, the vdW energy difference is very small, even smaller in the 100 K derived structure, and it is primarily the difference in $E_{\text{el,ind}}$ that is fundamental to obtain the correct energetic order. The reason for this is that in the highly symmetric α phase, the induced electrostatic energy is negligible or very small (100 K structure) while in the anisotropic δ phase, the induced dipoles and thus $E_{\text{el,ind}}$ are substantial. This clearly demonstrates that the inclusion of effects due to induced electrostatic contributions, such as in the *pol* FF, is fundamental for a correct description of the energetic ordering of the two phases.

Table 3: Total energy and its contributions (in kcal/mol per s.u.) of the α and δ phase optimized with the *npol* and *pol* models at 0K. For the α phase the column labeled by (exp.) corresponds to the re-optimized experimental structure, while the one labeled (100 K) refers to the structure obtained from the optimization of the frames of the 100 K trajectory. The energy difference is computed as $\Delta E = E_{\alpha} - E_{\delta}$.

<i>npol</i>					
	α phase (exp.)	α phase (100 K)	δ phase	ΔE (exp.)	ΔE (100K)
E_{tot}	-172.90	-174.17	-173.26	0.36	-0.91
E_{vdW}	3.78	3.29	2.38	1.40	0.91
$E_{\text{el,perm}}$	-176.68	-177.46	-175.64	-1.04	-1.82
<i>pol</i>					
	α phase (exp.)	α phase (100 K)	δ phase	ΔE (exp.)	ΔE (100K)
E_{tot}	-258.10	-259.67	-262.09	3.99	2.42
E_{vdW}	12.62	12.02	12.01	0.61	0.01
$E_{\text{el,perm}}$	-270.72	-271.05	-265.79	-4.925	-5.26
$E_{\text{el,ind}}$	0.00	-0.64	-8.30	8.30	7.66

3.3 Finite temperature properties

3.3.1 Radial pair distribution functions

For NVT simulations we obtain (meta)stable phases at all investigated temperatures, while in the NPT simulations, only the *npol* model is able to generate α phase trajectories at 600 K and 650 K which do not melt (the experimental melting temperature is expected to be above 700 K⁴⁸).

To determine the ability of the *npol* and *pol* FFs in reproducing the structural properties of the DFT reference at finite temperature, we analyze the RPDFs of all systems for which the structures remained intact. Since, in the case of the classical MD simulations, the NPT trajectories are the most realistic ones, we will focus on these trajectories, the corresponding RPDFs of the NVT simulations are instead included in the Supporting Information (Figures S3-S8). Overall the differences between the two are minor.

In section 3.2.1 dedicated to the structural properties at 0 K, we have noted that both the *npol* and *pol* models can closely reproduce the RPDF at 0 K obtained from DFT data as well as the experimentally determined structure of the α phase. The same is observed at finite temperatures. In Figure 2, the RPDFs of the NPT-generated trajectories with the *npol* and *pol* models are plotted in comparison to DFT results at 650 K with fixed volumes V_0 and V_1 , respectively. The trajectories generated with the *npol* model at temperatures of 600 K and 650 K show a good agreement with the DFT results obtained for the expanded volume V_1 ($\Delta V = +21\%$, see Table 1). This is consistent with the supercell expansion observed at finite temperature (+15% at 600 K and +19% at 650 K, see Supporting Information Table S4). As for the 0 K case, the stable α phase trajectories produced with both the *npol* and *pol* FFs accurately reproduce the DFT reference, but only the *npol* model can generate stable trajectories for temperatures ≥ 600 K, i.e the temperature range for which, experimentally, the α phase is found to be more stable than the δ phase.^{22,23}

Similarly to what was observed already for the 0 K structures in Section 3.2.1, the results

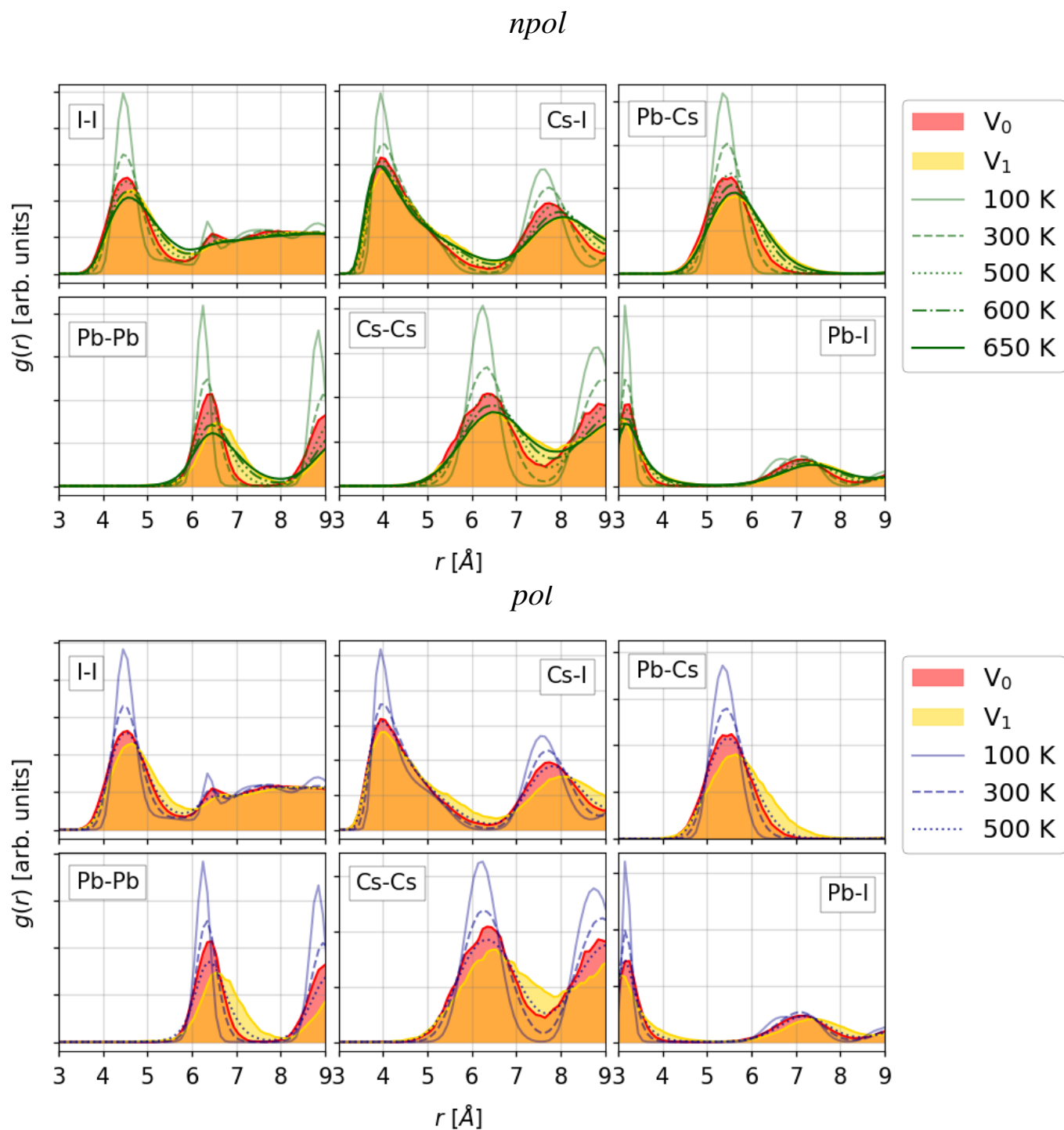


Figure 2: RPDFs of the α phase trajectories generated at different temperatures in the NPT ensemble. In the top panel, the RPDFs are shown for the *npol* model up to $T = 650\text{K}$. In the bottom panel, the RPDFs are shown for the *pol* model up to $T = 500\text{K}$, since for higher temperatures the system is melting. Note that the DFT RPDFs for the volume V_0 and V_1 , are computed from trajectories generated at 650K .

of the *npol* FF for the δ phase show some deviations with respect to the DFT reference. This is clear in the RPDFs at 100 K plotted in Figure 3. Figure 3 also shows that the *pol* model, on the other hand, reproduces the δ phase at 100 K in excellent agreement with respect to the DFT reference. The same is observed for higher temperatures for which the RPDFs are shown in the Supporting Information.

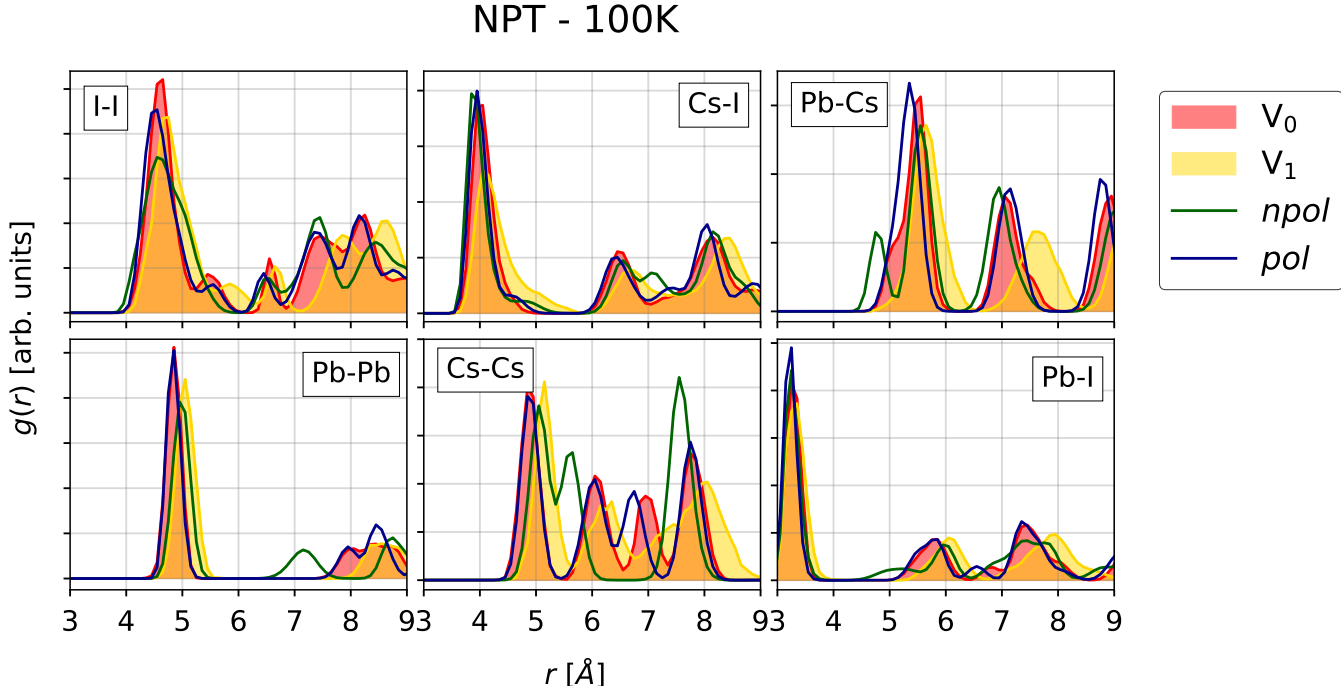


Figure 3: Comparison of radial pair distribution of DFT reference (V_0 and V_1), *npol* and *pol* NPT trajectories for the δ phase. All the trajectories are those simulated at 100 K.

3.3.2 Vibrational Properties

We also investigated the vibrational properties of α and δ phases of CsPbI_3 and compared the FF results with the DFT reference. In Figs. 4 and 5, we show the power spectra split into the contributions due to the individual species for δ and α CsPbI_3 , respectively, for trajectories generated with different methods, temperatures and cell volumes. Since CsPbI_3 is solely constituted by heavy elements, only very soft modes, in a region of $\sim 20\text{-}120\text{ cm}^{-1}$, are present, which is in agreement with the range typically observed for e.g. Pb-I skeleton

motions in MAPbI₃.^{68,69} Comparing the δ phase DFT power spectra at different volumes, we notice that the main effect of the volume expansion is a shift of modes involving Cs to the lower frequency, probably as a direct consequence of the increase of the space in between the edge-sharing Pb-I pillars in which the Cs ions can move. The main temperature effect is the appearance of a small diffusive component for $T \geq 300$ K, which is slightly more prominent in the V_0 trajectories. This is probably due to the fact that the cell volume is kept fixed, allowing for no thermal expansion. In the α phase, on the other hand, volume expansion shifts the modes around 50-80 cm⁻¹ assigned to Pb-I stretch vibrations⁶⁸ to lower frequency. For higher temperatures and expanded volumes, the spectra of the two phases get very similar. Comparing the power spectra of the FF trajectories with the ones of the DFT references, some discrepancies in the higher frequency range can be observed for the modes involving Pb and I. Whereas the DFT reference spectra extend to frequencies ≥ 100 cm⁻¹, the corresponding frequency range in the FF models reduces to around 10-80 cm⁻¹ in the *npol* and to 10-100 cm⁻¹ in the *pol* models. Also in this case, at high temperatures, the frequency range is shifted to a lower range and the δ and α phases' power spectra become more similar. Moreover, at high temperatures the differences between the results obtained with the *pol*, respectively *npol* models become smaller. In conclusion, neither of the FFs is able to fully reproduce the Pb and I modes in the higher frequency range suggesting that they are not able to fully describe the Pb-I stretch vibrations, but the *pol* FF including frequencies up to 100 cm⁻¹ provides a better match with respect to the DFT power spectra. In the Supporting Information, the species-resolved power spectra computed from the classical NVT trajectories as well as the total ones are given.

3.3.3 Energy analysis

As mentioned above, the structure of the α phase optimized starting from the experimental (fully cubic) data ends up in a local minimum. If one considers the (orthorhombic-like) α phase structure optimized starting from a 100 K frame, the correct relative energetic ordering

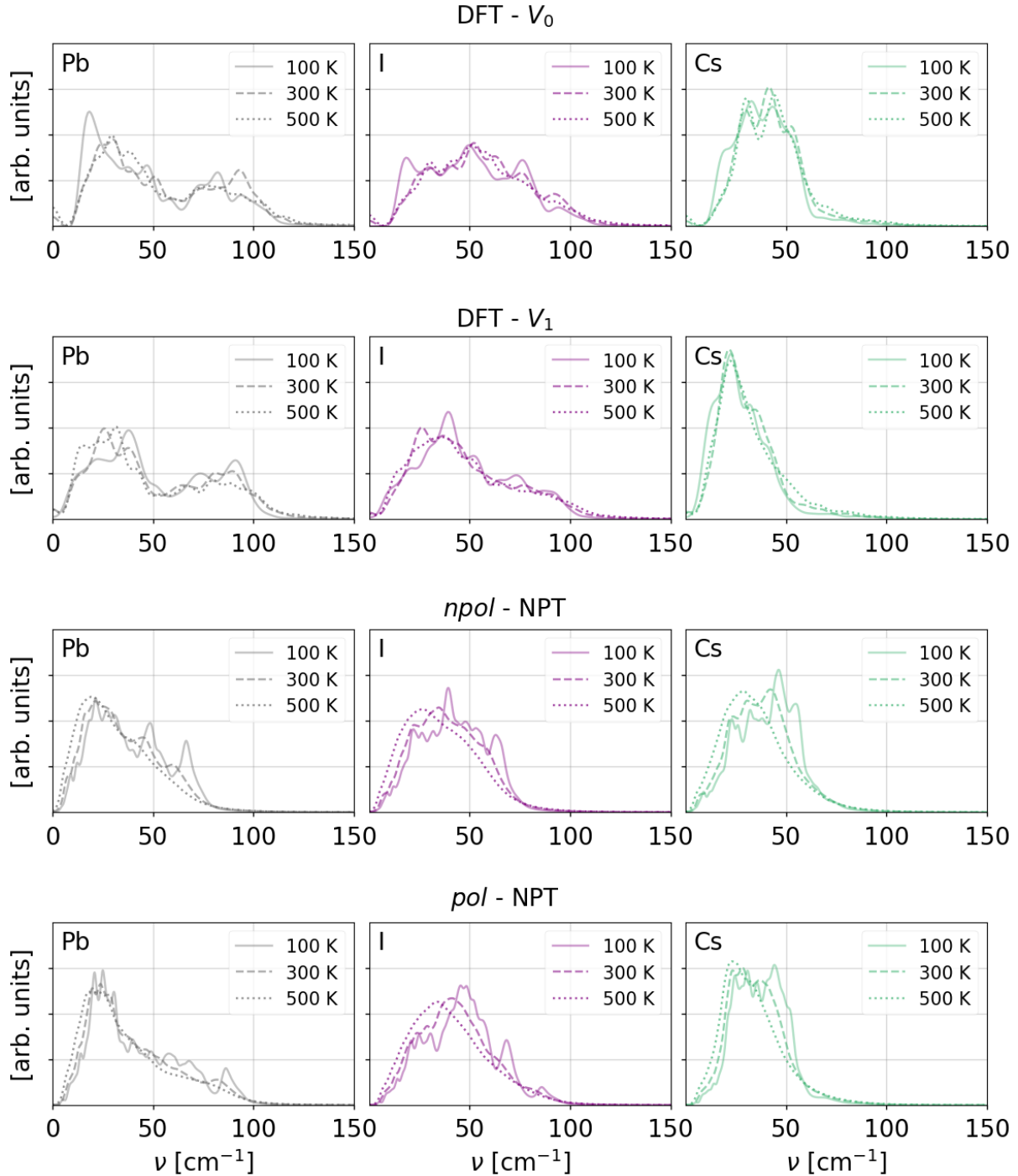


Figure 4: Species projected power spectra of δ CsPbI₃. The upper panels show the DFT power spectra up to 500 K for cells of volumes V_0 and V_1 . The lower panels show the power spectra of NPT trajectories generated with the *npol* and *pol* FFs. Note that for the FFs model we included trajectories up to 500 K.

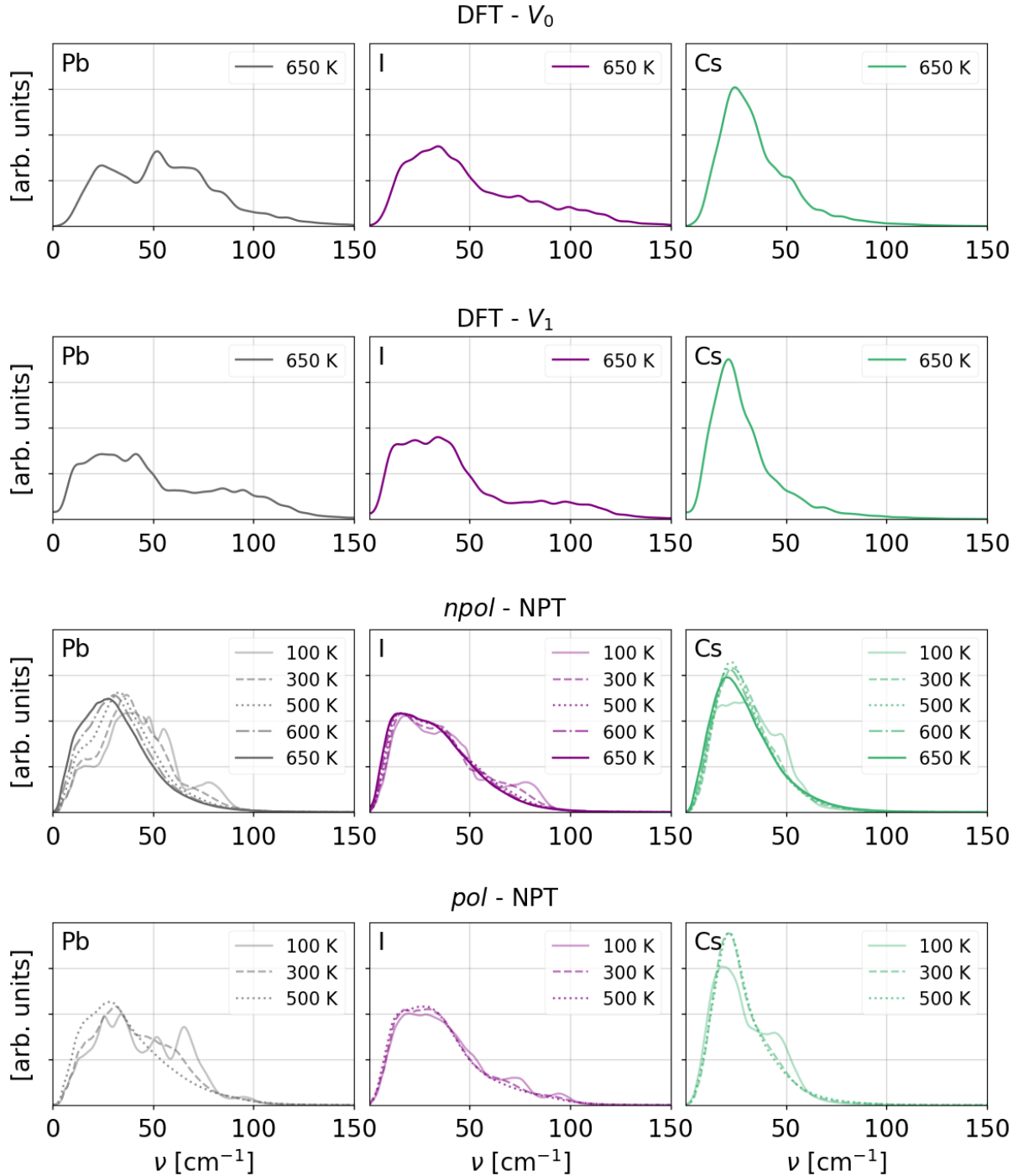


Figure 5: Species projected power spectra of α CsPbI₃. The upper panels show the DFT reference at 650 K for cell volumes V_0 and V_1 . The lower panels show the power spectra of NPT trajectories generated with the *npol* and *pol* FFs. For the *pol* model the power spectra are shown up to 500K, which is the higher temperature non-melting trajectory.

at 0 K, *i.e.* the δ phase being more stable than the α phase, is reproduced only by the *pol* model. Here, we study how the relative energetics of the two phases predicted by the two models change as a function of temperature. In Figure 6, the average total energy and its components from NPT trajectories at different temperatures are plotted (corresponding NVT results are given in the Supporting Information). Values of the α structure optimized from the experimental data are in gray to show the difference with respect to the results obtained with the 100 K optimized structure. The latter looks more consistent with the values at finite temperature. This is especially evident in the total energy and vdW terms.

In the *npol* model, the relative energetic order shows an α phase that is consistently more stable than the δ polymorph. On the contrary, in the *pol* model, the relative energetic ordering at low temperature is correctly reproduced and the energetic difference between the two phases steadily diminishes as a function of temperature. However, the α phase melts around 500K, *i.e.* before reaching the crossover point.

An analysis of the different energy contributions shows that in the *npol* model the vdW component favors the δ phase. However, differences in the vdW contribution are small in comparison to those of the electrostatic energy, which preferentially stabilizes the α structure. Also in the *pol* model, the electrostatic interactions at finite temperature favor α , whereas the energy differences in the vdW contribution are so small that we cannot determine for sure which phase they would favor. The decisive contribution to the relative energetics and its thermal evolution is by far the induced electrostatic term. Due to the inherent structural anisotropy, the δ phase has a much higher contribution of E_{ind} than the α phase, which due to its high cubic symmetry has essentially no contributions from the induced dipole interaction at low temperature. For both phases, the magnitude of the induced electrostatic interactions becomes larger with increasing thermal fluctuations. However, due to the breaking of the initial high symmetry, the thermal increase in E_{ind} is more rapid for the α leading to an overall reduction of the average energy difference between the two phases and promoting a phase transition. The different trend observed for the energy contributions of the *npol*

model, in particular for the vdW term that stabilizes the δ phase, is due to the missing polarizability, which as just discussed is fundamental for obtaining the right energetic order.

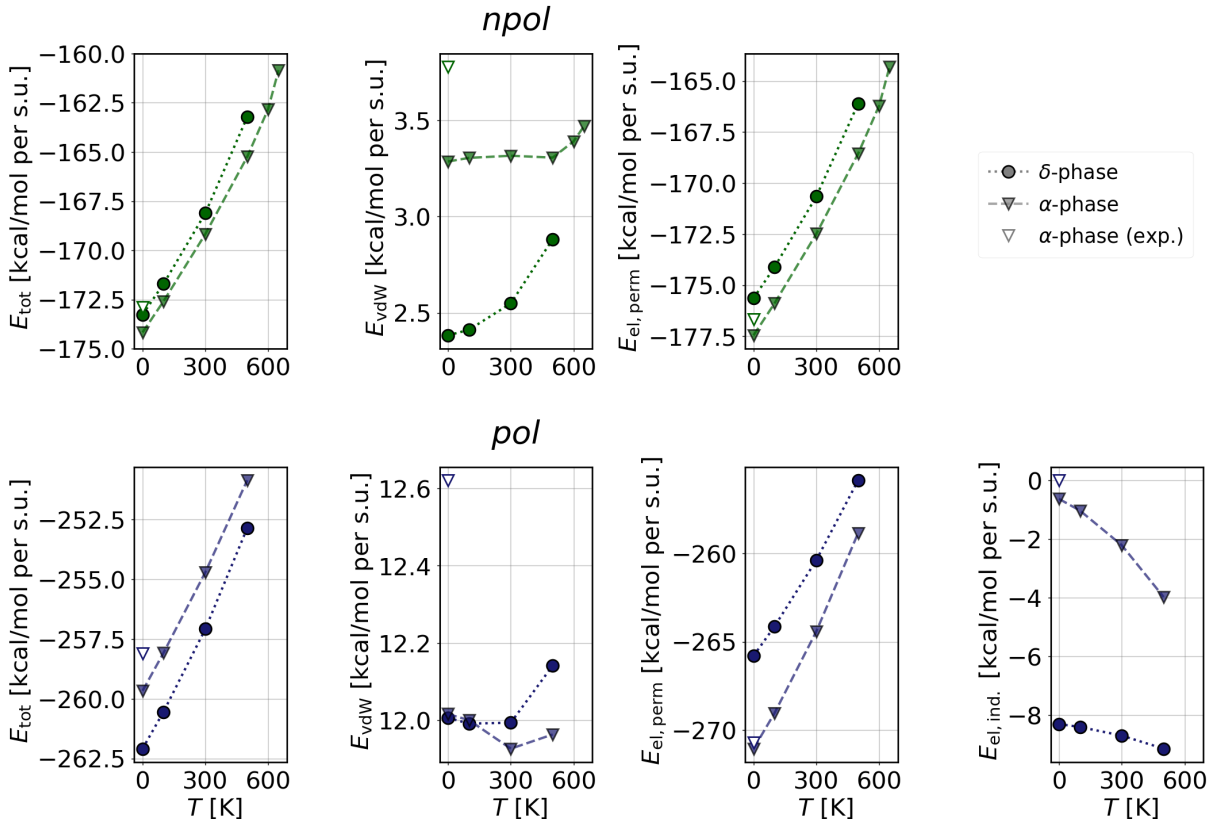


Figure 6: Average total energies and energy contributions of the classical NPT trajectories at finite temperatures of the δ and α phases of CsPbI_3 . The empty points show the energy contribution of the α phase optimized from the experimental structure.

4 Conclusions

Here, we presented a force matching approach for the semi-automated generation of a fixed-point charge *npol* as well as for a polarizable *pol* FF for the all inorganic perovskite CsPbI_3 based on extensive data from DFT based molecular dynamics simulations. We find that both models are able to reproduce the overall structural features of the δ as well as the α phase. In particular, if one is interested in the properties of the perovskite phase alone, the *npol* FF developed here offers a viable and computationally efficacious option. However, some subtle

structural details of the highly-anisotropic δ phase are better reproduced with the *pol* model, a trend that is also reflected in a better reproduction of the vibrational properties. Remarkably, the relative phase stability of the two polymorphs is only captured by the *pol* model. In fact, it turns out that the decisive component that governs the relative phase stability is the electrostatic interactions due to induced dipoles. At lower temperatures, this contribution is stabilizing the anisotropic δ phase over the α phase, for which the E_{ind} contribution is essentially zero due to the high symmetry. However, this contribution increases rapidly at elevated temperatures due to the symmetry breaking by thermal fluctuations. Clearly, these interactions cannot be captured with a *npol* model. In fact, within the *npol* model, these crucial force contributions can only be mimicked (and only partially be accounted for) by an effective vdW term. In other words, *npol* force fields have to describe the relative energetic difference between α and δ phases based ‘on the wrong physics’, which clearly hampers their viability and scope. The finding that the presence and magnitude of induced dipoles is the crucial factor that influences the relative energetics of δ versus α phase is most likely not limited to the δ/α polymorphism in CsPbI₃ but seems also applicable to other systems such as FAPbI₃ and can thus provide some rational guidance for synthetic attempts in stabilizing the photoactive α phase. In fact, this result suggests that breaking the symmetry of the cubic phase by introducing anisotropy will help in shifting the relative phase equilibrium towards the α phase. This paradigm is indeed consistent with and is able to rationalize a number of experimental observations such as the fact that at low temperatures orthorhombic perovskite phases are usually more stable than the cubic ones;⁴ the presence of a more anisotropic monovalent cation like FA leads to a lowering of the phase transition temperature (FAPbI₃ 418K⁷⁰ versus 600K for CsPbI₃^{22,23}); and the introduction of different monovalent cations and/or other halides in mixed cation/halide perovskites can be used to stabilize the α phase.^{8,71–73}

Acknowledgment

C.V. gratefully acknowledges a INSPIRE Potentials - MARVEL Master's Fellowship from the NCCR MARVEL. U.R. acknowledges funding from the Swiss National Science Foundation via grant No. 200020219440 and computational resources from the Swiss National Supercomputing Centre CSCS.

Data availability

Data and analysis scripts are available on Zenodo at <https://doi.org/10.5281/zenodo.11175491>. Additionally, on Zenodo the link to the GitHub repository containing the interface for performing the force matching is provided.

References

- (1) Laboratory, N. R. E. Best Research Cell Efficiencies. 2019; <https://www.nrel.gov/pv/cell-efficiency.html>.
- (2) Kojima, A.; Teshima, K.; Shirai, Y.; Miyasaka, T. Organometal Halide Perovskites as Visible-Light Sensitizers for Photovoltaic Cells. *Journal of the American Chemical Society* **2009**, *131*, 6050–6051.
- (3) Min, H.; Lee, D. Y.; Kim, J.; Kim, G.; Lee, K. S.; Kim, J.; Paik, M. J.; Kim, Y. K.; Kim, K. S.; Kim, M. G. et al. Perovskite solar cells with atomically coherent interlayers on SnO₂ electrodes. *Nature* **2021**, *598*, 444–450.
- (4) Stoumpos, C. C.; Malliakas, C. D.; Kanatzidis, M. G. Semiconducting Tin and Lead Iodide Perovskites with Organic Cations: Phase Transitions, High Mobilities, and Near-Infrared Photoluminescent Properties. *Inorganic Chemistry* **2013**, *52*, 9019–9038.

- (5) Ahmad, W.; Khan, J.; Niu, G.; Tang, J. Inorganic CsPbI₃ Perovskite-Based Solar Cells: A Choice for a Tandem Device. *Solar RRL* **2017**, *1*, 1700048.
- (6) Wang, D.; Yao, S.; Zhong, Y.; Peng, L.; Shi, T.; Chen, J.; Liu, X.; Lin, J. Optoelectronic simulation of a four-terminal all-inorganic CsPbI₃/CZTSSe tandem solar cell with high power conversion efficiency. *Physical Chemistry Chemical Physics* **2022**, *24*, 22746–22755.
- (7) Sim, K. M.; Swarnkar, A.; Nag, A.; Chung, D. S. Phase Stabilized α -CsPbI₃ Perovskite Nanocrystals for Photodiode Applications. *Laser & Photonics Reviews* **2018**, *12*, 1700209.
- (8) Saliba, M.; Matsui, T.; Seo, J.-Y.; Domanski, K.; Correa-Baena, J.-P.; Nazeeruddin, M. K.; Zakeeruddin, S. M.; Tress, W.; Abate, A.; Hagfeldt, A. et al. Cesium-containing triple cation perovskite solar cells: improved stability, reproducibility and high efficiency. *Energy & Environmental Science* **2016**, *9*, 1989–1997.
- (9) Gélvez-Rueda, M. C.; Ahlawat, P.; Merten, L.; Jahanbakhshi, F.; Mladenović, M.; Hinderhofer, A.; Dar, M. I.; Li, Y.; Dučinskas, A.; Carlsen, B. et al. Formamidinium-Based Dion-Jacobson Layered Hybrid Perovskites: Structural Complexity and Optoelectronic Properties. *Advanced Functional Materials* **2020**, *30*, 2003428.
- (10) Hong, L.; Milić, J. V.; Ahlawat, P.; Mladenović, M.; Kubicki, D. J.; Jahanbakhshi, F.; Ren, D.; Gélvez-Rueda, M. C.; Ruiz-Preciado, M. A.; Ummadisingu, A. et al. Guanine-Stabilized Formamidinium Lead Iodide Perovskites. *Angewandte Chemie International Edition* **2020**, *59*, 4691–4697.
- (11) Mishra, A.; Ahlawat, P.; Fish, G. C.; Jahanbakhshi, F.; Mladenović, M.; Almalki, M.; Ruiz-Preciado, M. A.; Gélvez-Rueda, M. C.; Kubicki, D. J.; Schouwink, P. A. et al. Naphthalenediimide/Formamidinium-Based Low-Dimensional Perovskites. *Chemistry of Materials* **2021**, *33*, 6412–6420.

- (12) Alanazi, A. Q.; Kubicki, D. J.; Prochowicz, D.; Alharbi, E. A.; Bouduban, M. E. F.; Jahanbakhshi, F.; Mladenović, M.; Milić, J. V.; Giordano, F.; Ren, D. et al. Atomic-Level Microstructure of Efficient Formamidinium-Based Perovskite Solar Cells Stabilized by 5-Ammonium Valeric Acid Iodide Revealed by Multinuclear and Two-Dimensional Solid-State NMR. *Journal of the American Chemical Society* **2019**, *141*, 17659–17669.
- (13) Su, T.-S.; Eickemeyer, F. T.; Hope, M. A.; Jahanbakhshi, F.; Mladenović, M.; Li, J.; Zhou, Z.; Mishra, A.; Yum, J.-H.; Ren, D. et al. Crown Ether Modulation Enables over 23% Efficient Formamidinium-Based Perovskite Solar Cells. *Journal of the American Chemical Society* **2020**, *142*, 19980–19991.
- (14) Krishna, A.; Zhang, H.; Zhou, Z.; Gallet, T.; Dankl, M.; Ouellette, O.; Eickemeyer, F. T.; Fu, F.; Sanchez, S.; Mensi, M. et al. Nanoscale interfacial engineering enables highly stable and efficient perovskite photovoltaics. *Energy & Environmental Science* **2021**, *14*, 5552–5562.
- (15) Masi, S.; Gualdrón-Reyes, A. F.; Mora-Seró, I. Stabilization of Black Perovskite Phase in FAPbI₃ and CsPbI₃. *ACS Energy Letters* **2020**, *5*, 1974–1985.
- (16) Mattoni, A.; Filippetti, A.; Saba, M. I.; Delugas, P. Methylammonium Rotational Dynamics in Lead Halide Perovskite by Classical Molecular Dynamics: The Role of Temperature. *The Journal of Physical Chemistry C* **2015**, *119*, 17421–17428.
- (17) Mattoni, A.; Filippetti, A.; Caddeo, C. Modeling hybrid perovskites by molecular dynamics. *Journal of Physics: Condensed Matter* **2017**, *29*, 043001.
- (18) Caddeo, C.; Saba, M. I.; Meloni, S.; Filippetti, A.; Mattoni, A. Collective Molecular Mechanisms in the CH₃NH₃PbI₃ Dissolution by Liquid Water. *ACS Nano* **2017**, *11*, 9183–9190.
- (19) Hata, T.; Giorgi, G.; Yamashita, K.; Caddeo, C.; Mattoni, A. Development of a Clas-

- sical Interatomic Potential for MAPbBr₃. *The Journal of Physical Chemistry C* **2017**, *121*, 3724–3733.
- (20) Jinnouchi, R.; Lahnsteiner, J.; Karsai, F.; Kresse, G.; Bokdam, M. Phase Transitions of Hybrid Perovskites Simulated by Machine-Learning Force Fields Trained on the Fly with Bayesian Inference. *Physical Review Letters* **2019**, *122*, 225701.
- (21) Bokdam, M.; Lahnsteiner, J.; Sarma, D. D. Exploring Librational Pathways with on-the-Fly Machine-Learning Force Fields: Methylammonium Molecules in MAPbX₃ (X = I, Br, Cl) Perovskites. *The Journal of Physical Chemistry C* **2021**, *125*, 21077–21086.
- (22) Beal, R. E.; Slotcavage, D. J.; Leijtens, T.; Bowring, A. R.; Belisle, R. A.; Nguyen, W. H.; Burkhard, G. F.; Hoke, E. T.; McGehee, M. D. Cesium Lead Halide Perovskites with Improved Stability for Tandem Solar Cells. *The Journal of Physical Chemistry Letters* **2016**, *7*, 746–751.
- (23) Marronnier, A.; Roma, G.; Boyer-Richard, S.; Pedesseau, L.; Jancu, J.-M.; Bonnassieux, Y.; Katan, C.; Stoumpos, C. C.; Kanatzidis, M. G.; Even, J. Anharmonicity and Disorder in the Black Phases of Cesium Lead Iodide Used for Stable Inorganic Perovskite Solar Cells. *ACS Nano* **2018**, *12*, 3477–3486.
- (24) Stoumpos, C. C.; Kanatzidis, M. G. The Renaissance of Halide Perovskites and Their Evolution as Emerging Semiconductors. *Accounts of Chemical Research* **2015**, *48*, 2791–2802.
- (25) Duan, J.; Zhao, Y.; He, B.; Tang, Q. High-Purity Inorganic Perovskite Films for Solar Cells with 9.72% Efficiency. *Angewandte Chemie International Edition* **2018**, *57*, 3787–3791.
- (26) Lai, H. M.; Lu, Z.; Choi, C. K. K.; Zhou, W.; Ngo Yau, C.; Tang, B. Z.; Ko, H. Direct Room Temperature Synthesis of α -CsPbI₃ Perovskite Nanocrystals with High Photolu-

- minescence Quantum Yields: Implications for Lighting and Photovoltaic Applications. *ACS Applied Nano Materials* **2022**, *5*, 12366–12373.
- (27) Almishal, S. S. I.; Rashwan, O. New accurate molecular dynamics potential function to model the phase transformation of cesium lead triiodide perovskite (CsPbI_3). *RSC Advances* **2020**, *10*, 44503–44511.
- (28) Wang, B.; Chu, W.; Tkatchenko, A.; Prezhdo, O. V. Interpolating Nonadiabatic Molecular Dynamics Hamiltonian with Artificial Neural Networks. *The Journal of Physical Chemistry Letters* **2021**, *12*, 6070–6077.
- (29) Rathnayake, P. V. G. M.; Bernardi, S.; Widmer-Cooper, A. Evaluation of the AMOEBA force field for simulating metal halide perovskites in the solid state and in solution. *The Journal of Chemical Physics* **2020**, *152*, 024117.
- (30) Braeckevelt, T.; Goeminne, R.; Vandenhoute, S.; Borgmans, S.; Verstraelen, T.; Steele, J. A.; Roeffaers, M. B. J.; Hofkens, J.; Rogge, S. M. J.; Van Speybroeck, V. Accurately Determining the Phase Transition Temperature of CsPbI_3 via Random-Phase Approximation Calculations and Phase-Transferable Machine Learning Potentials. *Chemistry of Materials* **2022**, *34*, 8561–8576.
- (31) Ercolessi, F.; Adams, J. B. Interatomic Potentials from First-Principles Calculations: The Force-Matching Method. *Europhysics Letters (EPL)* **1994**, *26*, 583–588.
- (32) Ren, P.; Ponder, J. W. Polarizable Atomic Multipole Water Model for Molecular Mechanics Simulation. *The Journal of Physical Chemistry B* **2003**, *107*, 5933–5947.
- (33) Ponder, J. W.; Wu, C.; Ren, P.; Pande, V. S.; Chodera, J. D.; Schnieders, M. J.; Haque, I.; Mobley, D. L.; Lambrecht, D. S.; DiStasio, R. A. J. et al. Current Status of the AMOEBA Polarizable Force Field. *The Journal of Physical Chemistry B* **2010**, *114*, 2549–2564.

- (34) Rackers, J. A.; Wang, Z.; Lu, C.; Laury, M. L.; Lagardère, L.; Schnieders, M. J.; Piquemal, J.-P.; Ren, P.; Ponder, J. W. Tinker 8: Software Tools for Molecular Design. *Journal of Chemical Theory and Computation* **2018**, *14*, 5273–5289.
- (35) Yan, Z.; Zhai, W.; Wang, F.; Li, Q.; Lin, L.; Bao, C.; Zhang, C.; Gao, F.; Liu, J. M. Reversible Ionic Polarization in Metal Halide Perovskites. *The Journal of Physical Chemistry C* **2021**, *125*, 283–289.
- (36) Yaffe, O.; Guo, Y.; Tan, L. Z.; Egger, D. A.; Hull, T.; Stoumpos, C. C.; Zheng, F.; Heinz, T. F.; Kronik, L.; Kanatzidis, M. G. et al. Local Polar Fluctuations in Lead Halide Perovskite Crystals. *Physical Review Letters* **2017**, *118*, 136001.
- (37) Thole, B. Molecular polarizabilities calculated with a modified dipole interaction. *Chemical Physics* **1981**, *59*, 341–350.
- (38) Buckingham, R. The classical equation of state of gaseous helium, neon and argon. *Proceedings of the Royal Society of London. Series A. Mathematical and Physical Sciences* **1938**, *168*, 264–283.
- (39) Hill, T. L. Steric Effects. I. Van der Waals Potential Energy Curves. *The Journal of Chemical Physics* **1948**, *16*, 399–404.
- (40) Deretzis, I.; La Magna, A. Exploring the orthorhombic-tetragonal phase transition in $\text{CH}_3\text{NH}_3\text{PbI}_3$: the role of atom kinetics. *Nanoscale* **2017**, *9*, 5896–5903.
- (41) Li, Y.; Siegel, D. J.; Adams, J. B.; Liu, X.-Y. Embedded-atom-method tantalum potential developed by the force-matching method. *Physical Review B* **2003**, *67*, 125101.
- (42) Moré, J. J.; Garbow, B. S.; Hillstom, K. E. *User Guide for MINPACK-1*; Argonne National Laboratory Report ANL-80-74, 1980.
- (43) Moré, J. J.; Sorensen, D. C.; Hillstom, K. E.; Garbow, B. S. *Sources and Development of Mathematical Software*; Prentice-Hall, 1984; pp 88–111.

- (44) Giannozzi, P.; Baroni, S.; Bonini, N.; Calandra, M.; Car, R.; Cavazzoni, C.; Ceresoli, D.; Chiarotti, G. L.; Cococcioni, M.; Dabo, I. et al. QUANTUM ESPRESSO: a modular and open-source software project for quantum simulations of materials. *Journal of Physics: Condensed Matter* **2009**, *21*, 395502.
- (45) Perdew, J. P.; Burke, K.; Ernzerhof, M. Generalized Gradient Approximation Made Simple. *Physical Review Letters* **1996**, *77*, 3865–3868.
- (46) Rappe, A. M.; Rabe, K. M.; Kaxiras, E.; Joannopoulos, J. D. Optimized pseudopotentials. *Physical Review B* **1990**, *41*, 1227–1230.
- (47) Vanderbilt, D. Soft self-consistent pseudopotentials in a generalized eigenvalue formalism. *Physical Review B* **1990**, *41*, 7892–7895.
- (48) Trots, D.; Myagkota, S. High-temperature structural evolution of caesium and rubidium triiodoplumbates. *Journal of Physics and Chemistry of Solids* **2008**, *69*, 2520–2526.
- (49) Andreoni, W.; Curioni, A. New advances in chemistry and materials science with CPMD and parallel computing. *Parallel Computing* **2000**, *26*, 819–842.
- (50) Goedecker, S.; Teter, M.; Hutter, J. Separable dual-space Gaussian pseudopotentials. *Physical Review B* **1996**, *54*, 1703–1710.
- (51) Hartwigsen, C.; Goedecker, S.; Hutter, J. Relativistic separable dual-space Gaussian pseudopotentials from H to Rn. *Physical Review B* **1998**, *58*, 3641–3662.
- (52) Krack, M. Pseudopotentials for H to Kr optimized for gradient-corrected exchange-correlation functionals. *Theoretical Chemistry Accounts* **2005**, *114*, 145–152.
- (53) Nosé, S. A molecular dynamics method for simulations in the canonical ensemble. *Molecular Physics* **1984**, *52*, 255–268.
- (54) Hoover, W. G. Canonical dynamics: Equilibrium phase-space distributions. *Physical Review A* **1985**, *31*, 1695–1697.

- (55) Matsui, M.; Akaogi, M.; Matsumoto, T. Computational model of the structural and elastic properties of the ilmenite and perovskite phases of MgSiO_3 . *Physics and Chemistry of Minerals* **1987**, *14*, 101–106.
- (56) Pinilla, C.; Acuña Rojas, M.; Seriani, N.; Scandolo, S. An atomistic model of MgSiO_3 perovskite and post-perovskite phases. *Computational Materials Science* **2017**, *126*, 351–359.
- (57) Joung, I. S.; Cheatham, T. E. Determination of Alkali and Halide Monovalent Ion Parameters for Use in Explicitly Solvated Biomolecular Simulations. *The Journal of Physical Chemistry B* **2008**, *112*, 9020–9041.
- (58) Li, P.; Roberts, B. P.; Chakravorty, D. K.; Kenneth, M. M., Jr. Rational Design of Particle Mesh Ewald Compatible Lennard-Jones Parameters for +2 Metal Cations in Explicit Solvent. *Journal of Chemical Theory and Computation* **2013**, *9*, 2733–2748.
- (59) Feller, M. R.; Park, H.; Wilkins, J. W. Force-matched embedded-atom method potential for niobium. *Physical Review B* **2010**, *81*, 144119.
- (60) Ren, P.; Wu, C.; Ponder, J. W. Polarizable Atomic Multipole-Based Molecular Mechanics for Organic Molecules. *Journal of Chemical Theory and Computation* **2011**, *7*, 3143–3161.
- (61) Giannozzi, P.; Barone, G.; Bonfà, P.; Brunnauer, D.; Car, R.; Carnimeo, I.; Cavazzoni, C.; de Gironcoli, S.; Delugas, P.; Ferrari Ruffino, F. et al. Quantum ESPRESSO toward the exascale. *The Journal of Chemical Physics* **2020**, *152*, 154105.
- (62) Giannozzi, P.; Andreussi, O.; Brumme, T.; Bunau, O.; Buongiorno Nardelli, M.; Calandra, M.; Car, R.; Cavazzoni, C.; Ceresoli, D.; Cococcioni, M. et al. Advanced capabilities for materials modelling with Quantum ESPRESSO. *Journal of Physics: Condensed Matter* **2017**, *29*, 465901.

- (63) Henkelman, G.; Arnaldsson, A.; Jónsson, H. A fast and robust algorithm for Bader decomposition of charge density. *Computational Materials Science* **2006**, *36*, 354–360.
- (64) Humphrey, W.; Dalke, A.; Schulten, K. VMD: Visual molecular dynamics. *Journal of Molecular Graphics* **1996**, *14*, 33–38.
- (65) Brehm, M.; Kirchner, B. TRAVIS - A Free Analyzer and Visualizer for Monte Carlo and Molecular Dynamics Trajectories. *Journal of Chemical Information and Modeling* **2011**, *51*, 2007–2023.
- (66) Solomonik, V. G. The effective dipole polarizabilities of the ions in MX molecules: I. Alkali metal halides. *Journal of Structural Chemistry* **1979**, *19*, 860–866.
- (67) Hanni, M. E.; Keele, J. A.; Lundeen, S. R.; Fehrenbach, C. W.; Sturru, W. G. Polarizabilities of Pb^{2+} and Pb^{4+} and ionization energies of Pb^+ and Pb^{3+} from spectroscopy of high- L Rydberg states of Pb^+ and Pb^{3+} . *Physical Review A* **2010**, *81*, 042512.
- (68) Pérez-Osorio, M. A.; Milot, R. L.; Filip, M. R.; Patel, J. B.; Herz, L. M.; Johnston, M. B.; Giustino, F. Vibrational Properties of the Organic-Inorganic Halide Perovskite $\text{CH}_3\text{NH}_3\text{PbI}_3$ from Theory and Experiment: Factor Group Analysis, First-Principles Calculations, and Low-Temperature Infrared Spectra. *The Journal of Physical Chemistry C* **2015**, *119*, 25703–25718.
- (69) Mattoni, A.; Filippetti, A.; Saba, M.; Caddeo, C.; Delugas, P. Temperature Evolution of Methylammonium Trihalide Vibrations at the Atomic Scale. *The Journal of Physical Chemistry Letters* **2016**, *7*, 529–535.
- (70) Sturdza, B. K.; Gallant, B. M.; Holzhey, P.; Duijnste, E. A.; Von Der Leyen, M. W.; Sansom, H. C.; Snaith, H. J.; Riede, M. K.; Nicholas, R. J. Direct observation of phase transitions between delta- and alpha-phase FAPbI_3 via defocused Raman spectroscopy. *Journal of Materials Chemistry A* **2024**, *12*, 5406–5413.

- (71) Pellet, N.; Gao, P.; Gregori, G.; Yang, T.-Y.; Nazeeruddin, M. K.; Maier, J.; Grätzel, M. Mixed-Organic-Cation Perovskite Photovoltaics for Enhanced Solar-Light Harvesting. *Angewandte Chemie International Edition* **2014**, *53*, 3151–3157.
- (72) Boziki, A.; Mladenović, M.; Grätzel, M.; Rothlisberger, U. Why choosing the right partner is important: stabilization of ternary $\text{Cs}_y\text{GUA}_x\text{FA}_{(1-y-x)}\text{PbI}_3$ perovskites. *Physical Chemistry Chemical Physics* **2020**, *22*, 20880–20890.
- (73) Syzgantseva, O. A.; Saliba, M.; Grätzel, M.; Rothlisberger, U. Stabilization of the Perovskite Phase of Formamidinium Lead Triiodide by Methylammonium, Cs, and/or Rb Doping. *The Journal of Physical Chemistry Letters* **2017**, *8*, 1191–1196.